



## ISTITUTO NAZIONALE DI RICERCA METROLOGICA Repository Istituzionale

Numerical and Experimental Study of the Hydrostatic Pressure Correction in Gas Thermometry: A Case in the SPRIGT

This is the author's submitted version of the contribution published as:

*Original*

Numerical and Experimental Study of the Hydrostatic Pressure Correction in Gas Thermometry: A Case in the SPRIGT / Pan, Changzhao; Chen, Hui; Han, Dongxu; Zhang, Haiyang; Plimmer, Mark; Imbraguglio, Dario; Luo, Ercang; Gao, Bo; Pitre, Laurent. - In: INTERNATIONAL JOURNAL OF THERMOPHYSICS. - ISSN 0195-928X. - 41:8(2020). [10.1007/s10765-020-02686-9]

*Availability:*

This version is available at: 11696/64356 since: 2021-01-18T11:09:11Z

*Publisher:*

SPRINGER/PLENUM PUBLISHERS

*Published*

DOI:10.1007/s10765-020-02686-9

*Terms of use:*

This article is made available under terms and conditions as specified in the corresponding bibliographic description in the repository

*Publisher copyright*

SPRINGER

Copyright © Springer. The final publication is available at [link.springer.com](https://link.springer.com)

(Article begins on next page)

# Numerical and experimental study of the hydrostatic pressure correction in gas thermometry: A case in the SPRIGT

Changzhao Pan<sup>1,2, a)</sup>, Hui Chen<sup>1,3,4, a)</sup>, Dongxu Han<sup>5</sup>, Haiyang Zhang<sup>1,3</sup>, Mark Plimmer<sup>1,2</sup>,  
Dario Imbraguglio<sup>7</sup>, Ercang Luo<sup>1,3,6</sup>, Bo Gao<sup>1,3,6\*</sup>, Laurent Pitre<sup>1,2</sup>

<sup>1</sup> *TIPC-LNE Joint Laboratory on Cryogenic Metrology Science and Technology, Chinese Academy of Sciences (CAS), Beijing 100190, China*

<sup>2</sup> *LCM-LNE-Cnam, 61 rue du Landy, 93210 La Plaine-Saint Denis, France*

<sup>3</sup> *Key Laboratory of Cryogenics, Technical Institute of Physics and Chemistry, Chinese Academy of Sciences, Beijing, 100190, China*

<sup>4</sup> *Xi'an Jiaotong University, Xian 710049, China*

<sup>5</sup> *Beijing Institute of Petrochemical Technology, Beijing 102617, China*

<sup>6</sup> *University of Chinese Academy of Sciences, Beijing 100490, China*

<sup>7</sup> *Istituto Nazionale di Ricerca Metrologica, Strada delle Cacce 91, 10135 Torino, Italy*

## Abstract:

Single-pressure refractive-index gas thermometry (SPRIGT) is a new type of primary thermometry, which needs an extremely stable working pressure (stability <4 ppm). In practice, the pressure control system at room temperature is located above the cold resonator at 5 K to 25 K, and a long pressure-tube is used to connect them, which entails a hydrostatic pressure correction (HPC). To this end, a three-dimensional (3D) Computational Fluid Dynamics (CFD) simulation model of the pressure tube was developed and compared with experimental results. First, to verify the simulation results, the helium-4 gas pressure in the centre of the resonator was measured using a determination of the refractive index by microwave resonance coupled with a knowledge of the temperature. Results of simulation and experiment showed good agreement. Thereafter, based on this CFD simulation, the non-linear temperature distribution in the vertical pressure tube and the uncertainty caused by this non-linear phenomenon were calculated. After this, the validity of the isothermal assumption to simplify the calculation of the HPC was verified. Finally, the effect of heating on the pressure was studied and its impact found to be negligible. To the best of our knowledge, this is the first time experimental and simulation results have been compared for the HPC. The results are expected to be more generally applicable to the accurate determination of pressure in cryostats.

**Keywords:** primary thermometry, hydrostatic pressure correction, CFD, refractive index gas thermometry

---

\* Author to whom correspondence should be addressed. Electronic mail: bgao@mail.ipc.ac.cn;

1 a) These authors contributed to the work equally and should be regarded as co-first authors

2

### 3 **1. Introduction**

4 SPRIGT [1], single-pressure refractive-index gas thermometry, is a new type of gas  
5 thermometry. It is based on the measurement of the refractive index of a gas by microwave  
6 resonance in a suitably shaped resonator. For measurements in the temperature range 5 K to  
7 25 K, helium-4 is used as the thermometric gas. Compared with other types of refractive-index  
8 gas thermometry (RIGT) [2], the technique has the advantages of rapid measurement and only  
9 weak dependence on the accuracy of absolute pressure. It also allows tests of accurate *ab initio*  
10 calculations of helium-4 thermal properties. When copper is used as the resonator material (as  
11 in the present work), because its isothermal volumetric compressibility is almost constant with  
12 temperature in the range 5 K-25 K, SPRIGT measurements of the thermodynamic temperature  
13  $T$  can be very accurate (uncertainties better than 0.25 mK) and competitive with those using  
14 modern acoustic gas thermometry (AGT) [3].

15 SPRIGT requires three main sub-systems: a high thermal stability cryostat, a high accuracy  
16 microwave frequency measurement system and a gas-handling system allowing high purity,  
17 accurate pressure measurement and control. In previous work, we developed a cryogen-free  
18 cryostat cooled by a two-stage pulse tube cryocooler and demonstrated a temperature stability  
19 of 20  $\mu$ K for the range 5 K-25 K [4,5]. Thanks to this and the use of a quasi-spherical  
20 microwave resonator (QSR), a relative standard uncertainty of microwave frequencies can be  
21 measured in vacuum with relative standard uncertainties below 0.2 ppb [6]. In addition, a  
22 pressure control system was developed to reduce fluctuations below 0.1 ppm for helium-4 gas  
23 pressures from 30 kPa to 90 kPa at room temperature [7].

24 All the above achievements laid the foundations for the success of SPRIGT, but there  
25 remained the question of pressure calibration. The gas-handling system at room temperature is  
26 located above the cooled resonator, and a long pressure tube is needed to link the two. Given

1 the altitude and temperature differences, the effect of gravity is to generate a pressure  
2 differential between the gas-handling system and the resonator. To obtain the pressure inside  
3 the resonator, a hydrostatic pressure correction (HPC) must be applied.

4 The HPC is a common correction in several types of gas thermometry (such as constant  
5 volume gas thermometry CVGT [8,9,10], RIGT [2] and AGT [3]). Because it depends on two  
6 factors, namely the temperature profile along the tube and the altitude, its value can only be  
7 calculated by iteration. When the vapour pressure scales of the International Temperature of  
8 Scale of 1990 (ITS-90) were established, researchers usually only measured temperatures at  
9 several points along the pressure tube and used a linear approximation interpolation to calculate  
10 the HPC [8,9,10]. Some workers have tried to simplify the calculation of the HPC using designs  
11 incorporating short, high thermal conductivity vertical tubes separated by long, low thermal  
12 conductivity horizontal ones, such that temperature gradients occur only in the latter  
13 [11,12,13,14,15]. In all the above research however, the same problem persists, namely, that  
14 one can only use the temperature of the tube to replace the temperature of the working gas  
15 inside to calculate the HPC. In reality, because of heat losses caused by thermal conductivity  
16 and radiation, there exists a temperature difference between the tube surface and the working  
17 gas. This means such a method cannot be used to calculate the HPC with the accuracy required  
18 for thermometry at the 0.25 mK level of uncertainty.

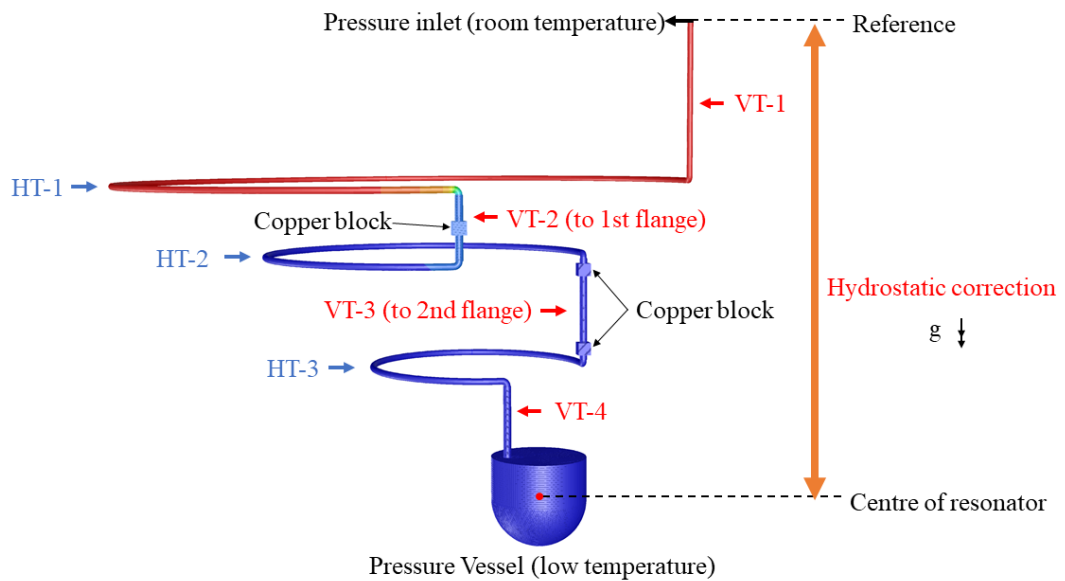
19 Computational fluid dynamics (CFD) provides an alternative way to solve the complex  
20 cryogenic problems related to fluid mechanics and heat transfer in the cryocooler, heat  
21 exchanger etc. [16,17,18]. Here we present a 3D CFD simulation model to calculate the HPC  
22 in a SPRIGT system and compare results with experiment.

23 The remainder of the paper is structured as follows. In the sections 2 and 3, the physical  
24 model of the pressure tube and the numerical settings in the simulation are presented. In section  
25 4, the HPC calculated using the simulation is compared with an experimental measurement of

1 pressure inferred from microwave refractive index, after which the modelled temperature  
2 distribution of the working gas is studied. Next, the different calculational models for the HPC  
3 are compared, and the error caused by using the traditional method is estimated. Finally, the  
4 heating effect on the pressure tube is studied.

5

## 6 2. Physical model



7

8 Figure 1. The simulation model uses a simplified structure for the pressure tube. HT:  
9 horizontal tube (stainless steel 316L); VT: vertical tube (OFHC copper, one surface of each  
10 block is thermally linked to a flange).

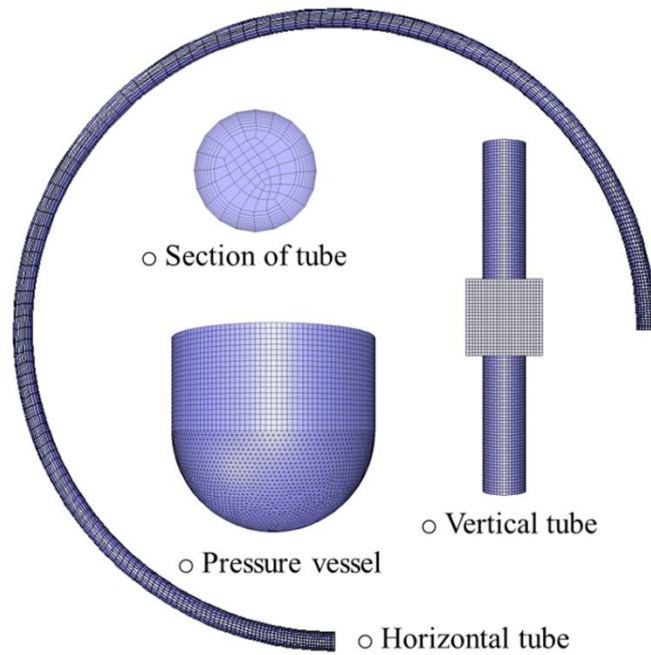


Figure 2. Meshes used for simulation of the pressure tube.

A detailed schematic of the cryostat can be found in a previous article [15]. The design of the pressure tube is similar to that of Sparasci *et al.* [12,13,14] used in a helium-3 and helium-4 vapour pressure system. The inlet located on the top flange leads to the pressure control system at room temperature. From the top flange down to the pressure vessel, the pressure tube is made from two kinds of material according to its position. The *altitude* is bridged by four short vertical tubes (VT-1 to VT-4) made from high thermal conductivity copper. The *temperature gradient* is established by the three long horizontal low thermal conductivity stainless steel tubes (HT-1 to HT-3) that link them. This design helps maintain the working gas located at different altitudes at a constant temperature while that at different temperatures is kept at the same altitude. In principle, such a design simplifies the calculation of the HPC [11,12,13,14].

1 Table 1 Dimensions of vertical (VT) and horizontal tubing (HT) sections used for the simulation  
 2 model and boundary conditions. All tubes have the same inner diameter of 12 mm.

Segment	Length / mm	Wall thickness / mm	Material	Position	Boundary condition
VT-1	355	0.2	Stainless steel	Vertical	Adiabatic <sup>1</sup>
VT-2	138	1	Copper		Thermal link to the 1 <sup>st</sup> flange <sup>2</sup>
VT-3	225	1	Copper		Thermal link to the 2 <sup>nd</sup> flange <sup>3</sup>
VT-4	145	1	Copper		Isothermal (working temperature)
HT-1	3000	0.2	Stainless steel	Horizontal	Adiabatic <sup>1</sup>
HT-2	1500	0.2	Stainless steel		Adiabatic <sup>1</sup>
HT-3	1000	0.2	Stainless steel		Adiabatic <sup>1</sup>
Pressure vessel	95 (to centre)	5	Copper	-	Isothermal (working temperature) <sup>4</sup>

- 3 1. The adiabatic boundary condition means the heat-flux from radiation is neglected. In the experiment, the vertical tube is  
 4 protected by the radiation shield, and the radiation heat loss can only change the temperature profile along the horizontal  
 5 tube. Thus, the radiation has only a very small influence on the HPC.  
 6 2. Its temperature value is taken from the experiment result. In this simulation, it is set to 63.7900 K at 30 kPa, 63.9243 K at  
 7 60 kPa and 60.484 K at 90 kPa.  
 8 3. Two thermal links were used to link with the second flange. In this simulation, the temperature of the upper one is set to  
 9 24.8645 K at 30 kPa, 24.9182 K at 60 kPa and 24.9605 K at 90 kPa; that of the lower one is set to 24.5462 K at 30 kPa,  
 10 24.5495 K at 60 kPa and 24.5528 K at 90 kPa.  
 11 4. In this simulation, it is set to 24.5552 K at 30 kPa, 24.55546 K at 60 kPa and 24.55542 K at 90 kPa.  
 12

13 In practice, the simulation model was simplified to that shown in figures 1 and 2. For  
 14 the vertical tube VT-2, a copper block was incorporated to provide a thermal link, while for the  
 15 tube VT-3, two copper blocks were installed. The surface of each block was assigned the same  
 16 constant temperature as the flange to which it was linked. The horizontal tube was represented  
 17 by a three-quarter circular arc to approximate the actual coil tube. Details of each component  
 18 are listed in table 1.

### 19 3. Mathematical model and numerical method

21 The behaviour of the working gas is governed by conservation equations for mass (1),  
 22 momentum (2), and energy (3):

$$23 \frac{\partial \rho}{\partial t} + \nabla \cdot (\rho \vec{V}) = 0 \quad (1)$$

$$24 \rho \frac{\partial \vec{V}}{\partial t} + \nabla [\vec{V} \cdot (\rho \vec{V})] = -\nabla p - \frac{2}{3} \nabla [\mu (\nabla \cdot \vec{V})] + \nabla \cdot [\mu (\nabla \vec{V})^T] + \nabla \cdot [\mu (\nabla \vec{V})] \quad (2)$$

$$25 \rho C_p \frac{\partial T}{\partial t} + \rho C_p \vec{V} \cdot \nabla T = \nabla \cdot [\lambda (\nabla T)] + \left[ \frac{\partial p}{\partial t} + \vec{V} \cdot \nabla p \right] + \phi \quad (3)$$

1 where  $T$  is the thermodynamic temperature<sup>1</sup>,  $\rho$  the density,  $p$  the pressure,  $C_p$  the specific heat  
2 at constant pressure and  $\mu$  the dynamic viscosity, and  $\Phi$  is the dissipation function (or source  
3 term, the present simulation has no this item). These equations were solved using ANSYS<sup>TM</sup>  
4 Fluent 19.2 software (free academic version) [19].

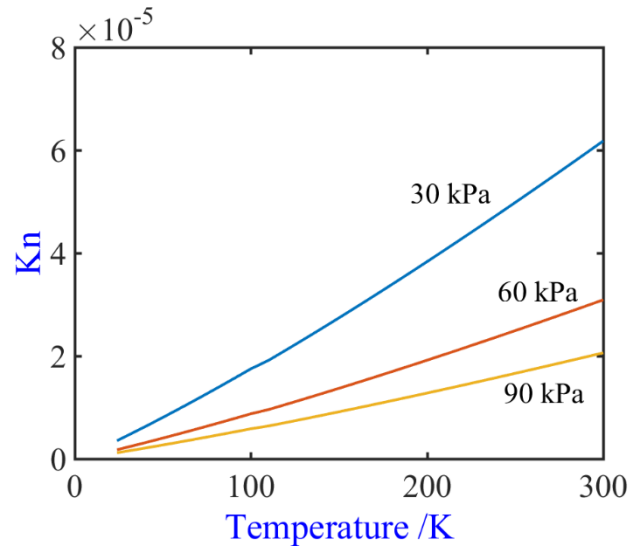
5 The temperature of the pressure tube and the working gas within it spans from 5 K to room  
6 temperature. To simulate the thermal behavior accurately, the temperature dependence of  
7 thermal properties must be included. The thermal properties of gaseous helium-4 were drawn  
8 from the NIST real gas model [20]. The thermal parameters of copper and stainless steel (from  
9 5 K to room temperature), calculated using the equations from NIST [21], were imposed by  
10 using the User Defined Function (UDF).

11 The boundary conditions were set as follows. The pressure at the inlet located on the top  
12 flange was set to a constant value, the size of which depends on the working pressure (here  
13 30 kPa, 60 kPa and 90 kPa). For the surface temperatures of the horizontal tubes and the vertical  
14 tube VT-1, adiabatic boundary conditions were imposed. Adiabatic boundary conditions were  
15 also imposed for the vertical tubes VT-2 and VT-3 except for the parts in contact with the  
16 surface of the block, where the boundary conditions were assumed to be isothermal. Isothermal  
17 boundary conditions were set too for the vertical tube VT-4 and the pressure vessel. Wherever  
18 possible, the temperature of each isothermal boundary value was drawn from to the measured  
19 experimental temperature of each part. The boundary conditions are summarized in Table 1. As  
20 shown in figure 3, the Knudsen number  $Kn$  [22] in all regions and for all pressure and  
21 temperatures explored in this simulation is lower than  $6 \times 10^{-5}$ , i.e. far less than 0.01, so the  
22 no slip boundary condition was used for all the surfaces of the pressure tube.

---

<sup>1</sup> The exponent  $T$  in equation 2 denotes the transpose of the matrix.





1

2 Figure 3. Variation of the Knudsen number  $Kn$  as function of temperature in the present  
3 simulation.

4

5

6

7

8

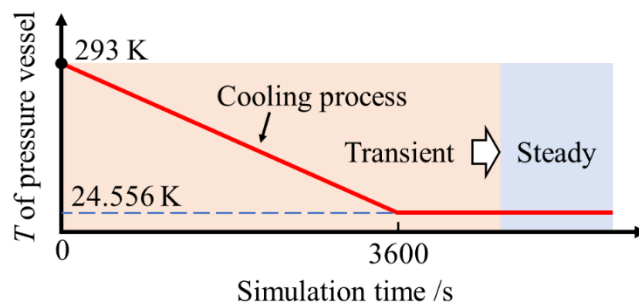
9

10

11

12

To make the simulation more stable, the initial condition was defined as the whole system being at 293 K under uniform pressure. As time evolves, the temperature of the isothermal boundary falls linearly to the stable temperature guided by the UDF (as shown in figure 4). A pressure and velocity coupling algorithm is employed to solve the transient equations (1) to (3) above. The convection terms are discretized using the second-order upwind scheme [23]. The time derivatives in equations 1 to 3 are discretized using a second-order implicit algorithm. The convergence tolerance of the energy equation is  $10^{-6}$  while for the other terms  $10^{-3}$  suffices. Using a computer with a 2.0 GHz processor and 2.0 GB RAM it took 3 to 4 days to obtain results for a given case.



13

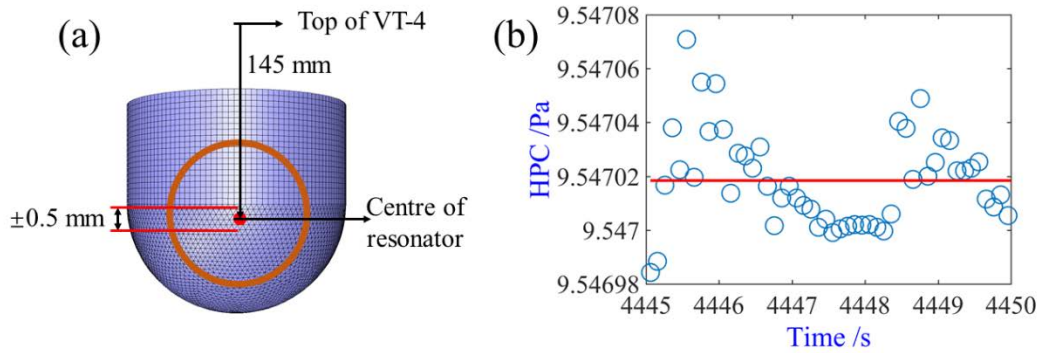
14

15

Figure 4. The process of simulation guided by the user-defined function.

#### 4. Results and discussion

#### 1 4.1 Estimating the uncertainty of the CFD simulation



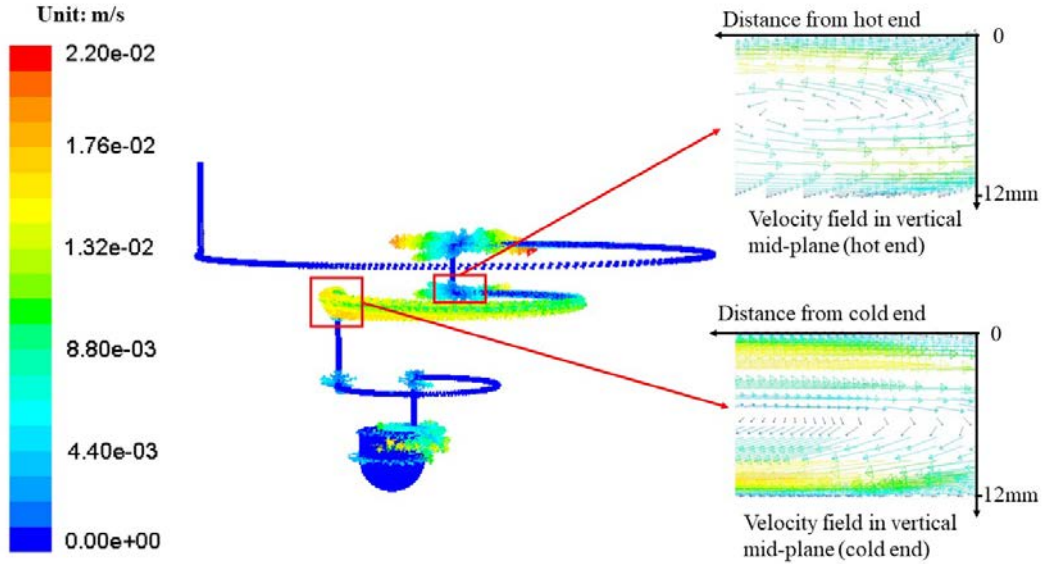
2

3 Figure 5. Sources of uncertainty in the simulation: (a) mesh size; (b) use of the steady-state  
4 algorithm.

5 To estimate the uncertainty of the present CFD simulation, the influence of two factors  
6 is considered: the mesh size and the state algorithm. Because the mesh size in the simulation is  
7 1 mm, the uncertainty in the altitude of the centre of the resonator can be as large as 0.5 mm,  
8 as shown in figure 5 (a). For a pressure of 90 kPa, this leads to an uncertainty in the HPC of  
9 9 mPa. On the other hand, as mentioned above, while the steady state was assumed in the  
10 simulation, there may exist transient conversion inside the pressure tube such as flow  
11 oscillations caused by thermoacoustic effects. To estimate the uncertainty caused by using the  
12 steady-state algorithm, a transient-state simulation was conducted and the evolution of the HPC  
13 with time obtained, as shown in figure 5 (b). For the transient state, the results showed it caused  
14 an uncertainty (standard deviation) for the HPC of only 0.018 mPa. Ultimately, the uncertainty  
15 in the simulation result is around 0.1 ppm for a pressure of 90 kPa.

16 Another factor influencing the simulation result is the convection caused by the  
17 temperature gradient and poorly fitting meshes. Even though the boundary-layer meshes and  
18 laminar viscous model were used to predict the possibility of thermoacoustic oscillation in the  
19 pressure tube, the tiny convection caused by the gravity and the interface of meshes increases  
20 the uncertainty of the simulation. Figure 6 shows the spatial velocity distribution in the pressure  
21 tube (case of 90 kPa). It is clear there is no large thermoacoustic oscillation in the tube and the

1 maximum velocity in the tube is at the level of  $10^{-2} \text{ m}\cdot\text{s}^{-1}$ . This velocity corresponds to a dynamic  
 2 pressure of 0.2 mPa, which can be regarded as the uncertainty caused by the convection. Figure  
 3 6 also shows the flow pattern at the both ends of HT-2, which is similar to the result shown in  
 4 the reference [24] figure 12.



5  
 6 Figure 6. The velocity in the pressure tube in units of  $\text{m}\cdot\text{s}^{-1}$  (typical result for 90 kPa).

## 8 4.2 Validation of simulation results

9 To validate the simulation results, it is necessary to know the pressure both at the top of  
 10 pressure tube and in the centre of the resonator. Here the pressure at the top is measured using  
 11 a piston gauge as in our previous work [7], while the pressure in the centre of the resonator can  
 12 be obtained from the refractive index gas via microwave resonance and a knowledge of the gas  
 13 temperature measured by contact thermometry. The following equations (derived in  
 14 Supplementary Material) were used to obtain the pressure in the resonator from the  
 15 experimental mode frequencies [2][25][26]:

$$16 \quad n(T, p) = \frac{\langle f + \Delta f \rangle_0}{\langle f + \Delta f \rangle_p (1 - \kappa_T p / 3)} \quad (4)$$

$$17 \quad n^2(T, p) - 1 = A_n(T)p + B_n(T)p^2 + C_n(T)p^3 + D_n(T)p^4 \dots \quad (5)$$

1 in which:

$$2 \quad A_n(T) = \frac{3}{RT} (A_\epsilon + A_\mu) \quad (6)$$

$$3 \quad B_n(T) = \frac{3}{R^2 T^2} (A_\epsilon^2 + B_\epsilon - A_\epsilon B_\rho - A_\mu B) \quad (7)$$

$$4 \quad C_n(T) = \frac{3}{R^3 T^3} (A_\epsilon^3 + 2A_\epsilon B_\epsilon + C_\epsilon - 2A_\epsilon^2 B_\rho - 2B_\epsilon B_\rho + 2A_\epsilon B_\rho^2 - A_\epsilon C_\rho - A_\mu C) \quad (8)$$

$$5 \quad D_n(T) = \frac{3}{R^4 T^4} (A_\epsilon^4 + 3A_\epsilon^2 B_\epsilon + B_\epsilon^2 + 2A_\epsilon C_\epsilon - A_\epsilon^2 B^2 - B_\epsilon B^2 + A_\epsilon B^3 + A_\mu B^3 - 2A_\epsilon^2 C - 2B_\epsilon C +$$
$$6 \quad 2A_\epsilon B C + 2A_\mu B C + D_\epsilon - A_\epsilon D - A_\mu D - 3A_\epsilon^3 B - 6A_\epsilon B_\epsilon B - 3C_\epsilon B + 6A_\epsilon^2 B^2 + 6B_\epsilon B^2 - 6A_\epsilon B^3 -$$
$$7 \quad 6A_\mu B^3 + 3A_\epsilon B C + 3A_\mu B C). \quad (9)$$

8 Here  $\kappa_T$  is the compressibility of the resonator,  $A_\epsilon$ ,  $B_\epsilon$ , and  $C_\epsilon$  are the dielectric virial  
9 coefficients,  $A_\mu$  is the first diamagnetic virial coefficient, and  $B$ ,  $C$ ,  $D$  are the density virial  
10 coefficients, In the calculation, the value of  $\kappa_T$  is calculated by the equation used in the  
11 reference [26] and the properties of copper in references [27][28]. The above virial coefficients  
12 are drawn from *ab initio* calculation results [29,30,31,32]. In equations (4) to (9), the only  
13 unknown value is the pressure. In the SPRIGT experiment, the temperature of the resonator  
14 was measured using a rhodium-iron resistance thermometer (RIRT) calibrated by NPL [33]. To  
15 estimate the thermodynamic temperature, we used  $T_{90}$  and the estimation of  $T - T_{90}$  by the CCT  
16 Working Group 4 (WG4) [34]. The procedure for measurement of the resonance frequencies of  
17 the QSR was the same as in earlier work [3, 6].

18 The HPC in the experiment is calculated as follows. First, the pressure at room  
19 temperature ( $P_{room}$ ) is obtained by the piston gauge (Fluke PG 7601) used for pressure control.  
20 Secondly, the pressure in the centre of resonator ( $P_{resonator}$ ) is obtained by solving equations (4)  
21 and (5). The HPC is equal to

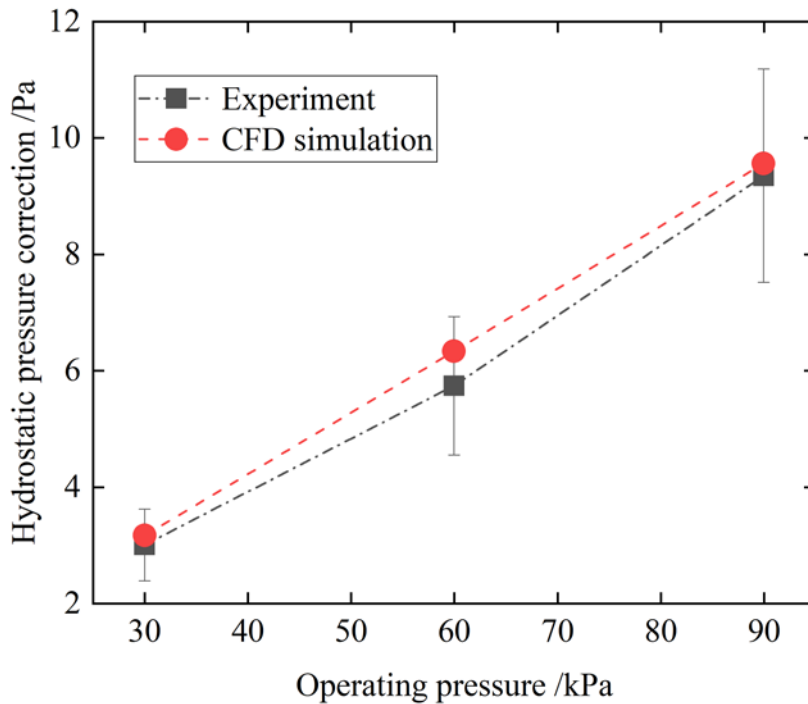
$$22 \quad HPC = P_{resonator} - P_{room} + \Delta P_{correction} \quad (10)$$

23 The term  $\Delta P_{correction}$  is mainly caused by the thermomolecular pressure difference (TPD),  
24 which can be calculated by [12] [35]:

1 
$$\Delta P = P_h - P_l = 2 \times 10^{-9} P_l (r \times P_l)^{-1.99} (T_h^{2.27} - T_l^{2.27}) \quad (11)$$

2 where  $P_h$ ,  $P_l$ ,  $T_h$ , and  $T_l$  refer to the pressures and temperatures at the high- and low-  
3 temperature extremities, respectively, of a tube of radius  $r$ . In the present work, the TPD mainly  
4 exists in the HT-1 and HT-2. The largest TPD occurs in HT-1 at 30 kPa, and its value is about  
5 0.75 mPa. The TPD is 10 000 times smaller than the HPC, and so can be neglected.

6 The detailed uncertainty budget for this process can be found in the Appendix. The  
7 experimental uncertainties include main components coming from the thermodynamic  
8 temperature measurement and the isothermal compressibility of copper, and lesser ones due to  
9 the dielectric virial coefficients, density virial coefficients etc. While the uncertainty in the  
10 pressure obtained in the present work (~20 ppm) is 10 times worse than the world's leading  
11 results [25], the purpose of this work is not to make the ultimate pressure standard; the results  
12 presented are perfectly adequate for a comparison with and validation of those of the simulation.  
13 Figure 7 shows the difference between the results of experiment and simulation at temperatures  
14 near the neon triple point (24.5561 K) for three operating pressures near 30 kPa, 60 kPa and  
15 90 kPa. The maximum differences are 0.161 Pa at 30 kPa, 0.591 Pa at 60 kPa and 0.209 Pa at  
16 30 kPa, all of which lie within the range of experimental uncertainty (as shown in the Appendix).  
17 We interpret this agreement as proof of the correctness of the present simulation.



1

2 Figure 7. Comparison between results of experiment and a simulation with computational  
 3 fluid dynamics. The dotted lines are added to guide the eye.

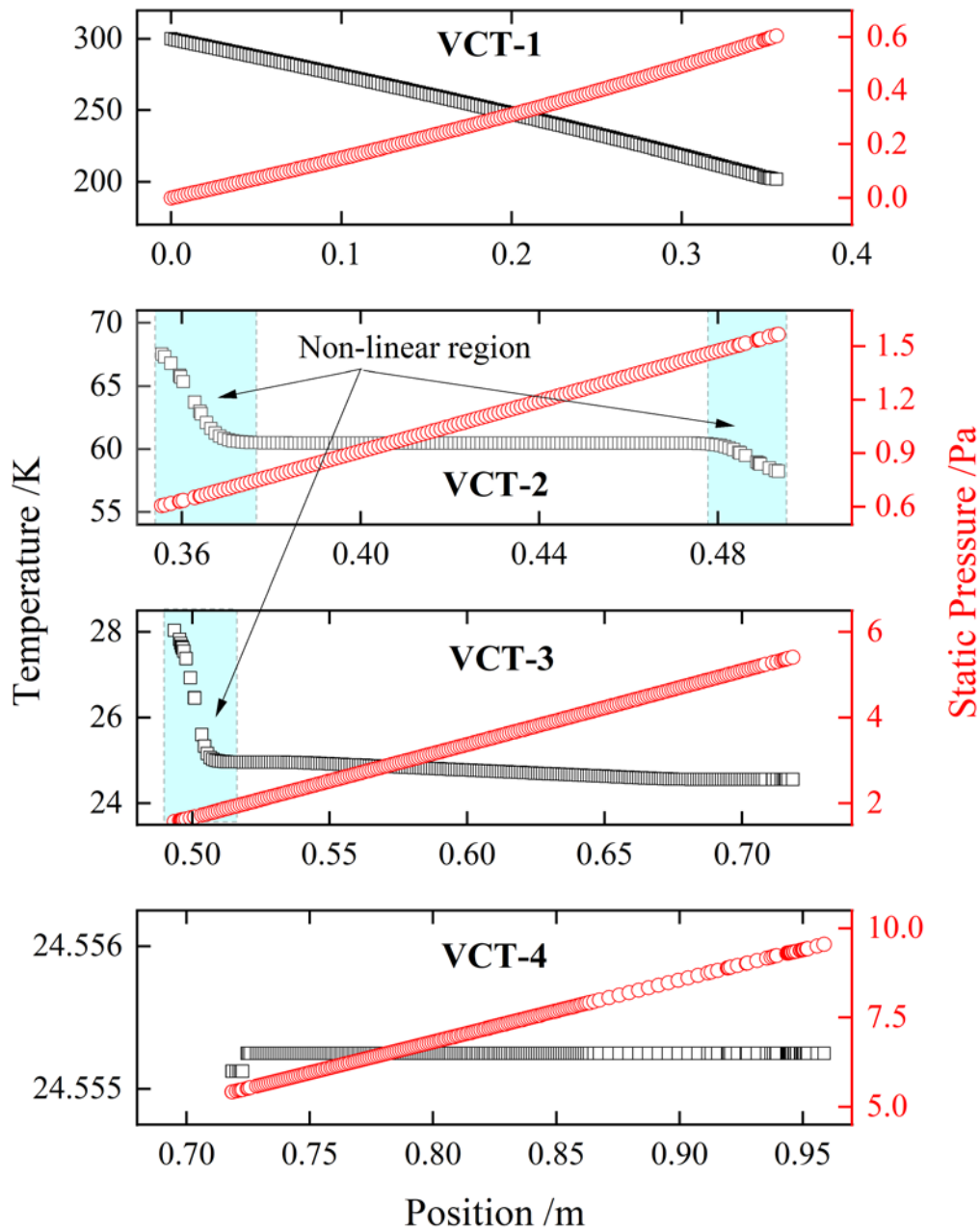
4 **4.3 Non-isothermal temperature distribution inside the pressure tube**

5 One of the advantages of using numerical simulation is that it can yield detailed  
 6 information that is hard to measure directly. In the experiment, one can only measure the (outer)  
 7 surface temperature of the pressure tube. Because of thermal losses, however, there exists a  
 8 temperature difference between the surface of the pressure tube and the working gas within it.  
 9 Using the (external) surface temperature of the pressure tube to approximate the temperature of  
 10 working gas will cause a bias. To quantify this shift, the temperature of working gas inside of  
 11 pressure tube should be modelled.

12 Figure 8 shows the typical temperature and pressure variation *versus* altitude in the  
 13 vertical pressure tubes VT-1, VT-2, VT-3 and VT-4 (from the top flange down to the centre of  
 14 the resonator). One can see that, even though high-conductivity copper was used for these tubes,  
 15 the temperature of the working gas inside them is still unlike that of the design condition: rather

1 than remaining constant it varies non-linearly over parts of certain tubing sections, notably VT-  
2 2 and VT-3 (see figure 8). There is a temperature gradient between the top and bottom ends of  
3 each vertical tube. The main heat transfer takes place at the extremities where the vertical tubes  
4 are connected to the horizontal ones. This is mainly due to the poor conductivity of low-pressure  
5 helium: it takes an ‘entrance distance’, labelled non-linear region in figure 8, to cool all the  
6 helium gas in the tube down to the surface temperature of pressure tube. For a more rigorous  
7 calculation of the HPC therefore, an exponential rather than a linear temperature distribution  
8 should be used in this region. In calculations carried out thus far, however [11][12], the  
9 isothermal assumption has always been made, so there will have been an error due to the  
10 nonlinear behavior being neglected.

11 On the other hand, because the vertical tube VT-1 is assumed to be adiabatic with no  
12 thermal link to keep it at a constant temperature, its temperature shows an almost linear  
13 variation with altitude. In the present experimental system, since no thermometers have yet  
14 been installed to measure this temperature distribution, an uncertainty is added to allow for a  
15 possible deviation from linearity. The following sub-section will give arguments to estimate by  
16 how much of the uncertainty will increase when the isothermal assumption is used to calculate  
17 the HPC.



1

2 Figure 8 Variation of temperature and pressure with altitude along the vertical pressure tube. The working  
 3 pressure is 90 kPa and the working temperature close to 24.5561 K (neon triple point). The position corresponds  
 4 to the altitude difference between the top of the pressure tube and the point shown. The kinks in the two middle  
 5 figures are reproduced by all three calculational methods and unlikely to result from a numerical artefact.

6

7 **4.4 Estimation of uncertainty due to non-isothermal behavior**



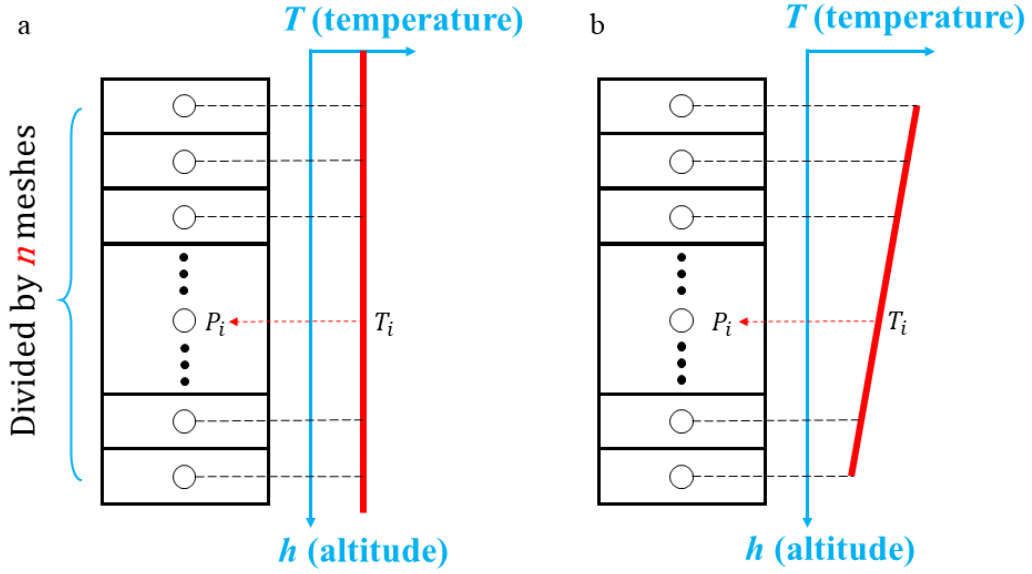


Figure 9 Meshes used to calculate the HPC a) Isothermal assumption: the vertical tube remains at a constant temperature  $T_i = T_0 \forall i$ ; b) Linear assumption: the vertical tube has linear temperature distribution.

In this part, calculations of the HPC using two different assumptions are compared with the results of the CFD simulation. In the first isothermal behavior is assumed while in the second, for VT-1 only, a linear temperature variation along the vertical tubing is assumed. The meshes are shown in figure 9 and the following iteration equations are used:

$$P_i = P_{i-1} + \rho_i g (h_i - h_{i-1}) \quad (12)$$

and  $P_i = RT_i [1 + B(T_i)\rho_i + C(T_i)\rho_i^2 + \dots]$  for the density  $\rho_i$ . Here  $B$  and  $C$  are the density virial coefficients, are drawn from [32], and  $g = 9.801\ 112\ 94\ (9.80E-07)\ \text{m s}^{-2}$  is the local value of the the gravitational acceleration in the laboratory at TIPC (Technical Institute of Physics and Chemistry) measured by scientists from the National Institute of Metrology of China (NIM). Here the uncertainty in the pressure is estimated by comparison of calculated values of the pressure with the simulation results.

Table 2 shows a comparison of results for the four vertical segments of the pressure tube. One sees that isothermal assumption causes a difference of 0.102 Pa (1.1 ppm) for VT-1, 0.005 Pa (0.05 ppm) for VT-2, 0.015 Pa (0.16 ppm) for VT-3 and 0.007 Pa (0.08 ppm) for VT-

1 4. The assumption of an isothermal temperature distribution along VT-1 contributes the largest  
 2 shift and the nonlinear temperature variation along VT-3 the second largest. The total difference  
 3 between the result of CFD simulation and that based on the isothermal assumption is only  
 4 around 0.83 ppm at 90 kPa. This means in practice one can use the isothermal assumption to  
 5 simplify the calculation of the HPC, a considerable saving in time.

6 In an effort to reduce the largest uncertainty, three different calculational models for the  
 7 HPC were intercompared - the CFD simulation, that using the isothermal assumption and that  
 8 using the linear assumption. Because no experimental data was available for the linear  
 9 assumption (specifically the temperature at the bottom of VT-1), the temperature predicted by  
 10 simulation (201 K) was used instead. When the linear assumption is used, the difference  
 11 between the result of the CFD simulation and the calculation is 0.005 Pa (0.06 ppm). Most of  
 12 this difference is caused by the non-linear temperature distribution along VT-2 and VT-3. In  
 13 future SPRIGT experiments, the uncertainty in the HPC will be reduced by measuring the  
 14 temperature at the bottom of VT-1 with a dedicated thermometer.

15

16 Table 2 Comparison of calculations of the HPC between CFD simulation, isothermal  
 17 assumption and linear assumption for the four vertical tubing segments VT-1 to VT-4.  
 18 (Working pressure 89 961.463 Pa and working temperature close to the neon triple point  
 19 24.5561 K)

Tubing segment	CFD simulation / Pa	Isothermal assumption / Pa	Linear assumption / Pa
VT-1	0.604	0.502	0.608
VT-2	0.962	0.967	0.931
VT-3	3.841	3.856	3.856
VT-4	4.140	4.147	4.147
Total	9.547	9.472	9.542

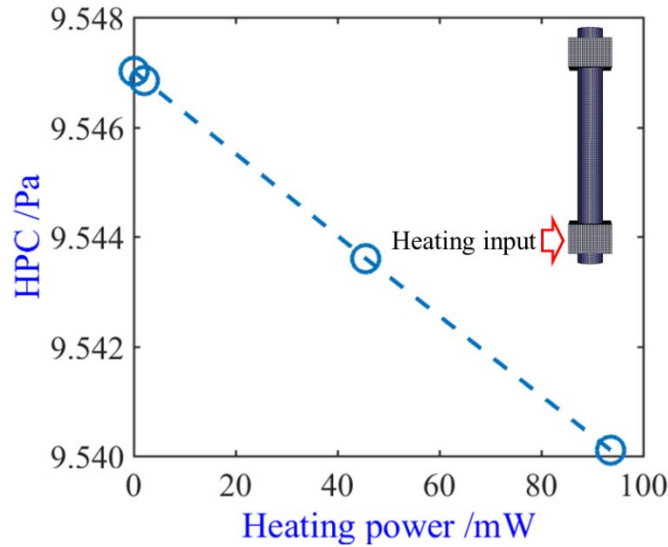
20

21 **4.5 Heating effect**

1           Any heat input to the pressure tube (e.g. via the flanges) influences the HPC and hence  
2 the calculated pressure at the centre of resonator, a knowledge of the zero of which is important  
3 in RIGT [2] and other low-temperature measurements [3,36]. To estimate this effect on the  
4 pressure tube, the effect of heating on the section VT-3 was simulated<sup>2</sup>. The results are shown  
5 in figure 10. One can see that the HPC falls linearly as the heating power is increased. For a  
6 power of 93 mW, the HPC only changes by around 0.007 Pa (0.08 ppm) at 90 kPa, which is  
7 even less than the shift due to non-isothermal behavior. The above results provide evidence that  
8 the correction due to the pressure tube is insensitive to the heating effect at this level. If the  
9 power supplied to VT-3 is less than 100 mW, this effect can be neglected. This conclusion is  
10 also supported by the experiment. In the SPRIGT experiment thus far, the heating effect has  
11 only been tested at 5 K, where it is larger than at 25 K. When about 20 mW of heating power  
12 is supplied to the pressure tube, the HPC changed around 42 mPa at 5 K. The density of helium  
13 at 5 K is more than five times higher than at 25 K, so at 25 K, the HPC should fall to about  
14 8 mPa. Even though the experimental value is much higher than that given by the simulation,  
15 this still shows that the effect of external heating can be neglected for powers below 100 mW.

---

<sup>2</sup> The reason for simulating VT-3 is that it is connected to the second flange of the cryostat and contributes greatly to the HPC, as shown in table 2.



1

2 Figure 8. Effect of external heating on the calculated hydrostatic pressure correction HPC.

3 Heat is applied via the contact block at the lower end of the third pressure tube VT-3, as  
 4 shown on the right).

### 5 **5. Conclusion**

6 In this paper, the hydrostatic pressure correction (HPC) in a cryostat close to 25 K was  
 7 evaluated. The motivation for the work is single-pressure refractive-index gas thermometry  
 8 (SPRIGT), in which an accurate knowledge of pressure is required to extract temperature values  
 9 from refractive index measurements. The pressure tube linking the resonator at the bottom of  
 10 the cryostat to a pressure gauge at the top was modelled using a computational fluid dynamics  
 11 simulation and the HPC calculated. Using this correction, the pressure in the centre of the  
 12 resonator could be predicted. To simplify calculation, the pressure tube was constructed as three  
 13 long horizontal sections linked by four short vertical ones, all tubes being of identical inner  
 14 diameter. To test the accuracy of the simulation, the pressure at the centre of a microwave  
 15 resonator was determined via microwave resonance measurement of the refractive index of  
 16 helium-4 gas, and a knowledge of its temperature (close to the neon triple point at 24.5561 K).  
 17 The experimental method is based on the fourth-order virial equation (A.11) linking pressure  
 18 and refractive index. The results of simulation and experiment showed good agreement. To the

1 best of our knowledge, this is the first time experimental and simulation results have been  
2 compared for the hydrostatic pressure correction.

3 Simulation results revealed a non-linear temperature distribution near the ends of the  
4 pressure tube, the effect of which is to increase by 0.83 ppm the error of the calculation HPC  
5 compared with the use of the isothermal assumption, as shown in section 4.4. At present,  
6 however, the largest source of uncertainty in the calculation of the HPC is the unknown  
7 temperature at the bottom end of the first vertical tubing section. This contribution could made  
8 negligible via the insertion of one of more thermometers to measure it. The effect of heating on  
9 the pressure tube was also simulated. The results showed that, for a heating power of 93 mW,  
10 the HPC only changes by around 0.007 Pa (0.08 ppm) at 90 kPa. This corresponds to a  
11 temperature shift of less than 1  $\mu$ K, which is negligible at the present level of uncertainty for  
12  $T_{SPRIGT}$ . The simulation results, validated by experiment, provide critical input for SPRIGT at  
13 low temperatures. Moreover, given the need to determine pressures accurately in cryostats  
14 worldwide, we believe the present work will have a broader impact.

15

## 16 **Acknowledgments**

17 This work was supported by the National Key R&D Program of China (Grant No.  
18 2016YFE0204200), the National Natural Science Foundation of China (Grant No. 51627809),  
19 the International Partnership Program of the Chinese Academy of Sciences (Grant No.  
20 1A1111KYSB20160017) and the European Metrology Research Programme (EMRP) Joint  
21 Research Project 18SIB02 “Real-K”. Changzhao Pan was supported by funding provided by a  
22 Horizon 2020 Marie Skłodowska Curie Individual Fellowship 2018 (No. 834024). The authors  
23 thank Duowu Su from NIM for the measurement of  $g$  at TIPC (Technical Institute of Physics  
24 and Chemistry, Chinese Academy of Sciences) in Langfang.

1 **Appendix Uncertainty budget for the determination of the HPC at the temperature of**  
 2 **the neon triple point**

3 References to the literature are given for the electromagnetic and density virial coefficients.

Working pressure	30 kPa	60 kPa	90 kPa
<i>Pressure in the resonator / Pa</i>			
<i>Uncertainty component, type B</i>			
<i>T of neon triple point</i>	0.527	0.998	1.530
$A_\epsilon$ [29]	0.003	0.007	0.01
$B_\epsilon$ [30]	0.048	0.187	0.422
$C_\epsilon$ [25]	0.001	0.004	0.014
$A_\mu$ [31]	0.002	0.001	0.001
B [32]	0.001	0.005	0.012
C [32]	-	-	-
D [32]	-	-	-
$\kappa_T$ [26-28]	0.051	0.105	0.157
<i>Uncertainty component, type A</i>			
$\langle f + g \rangle_0 / \langle f + g \rangle_p$	0.035	0.032	0.104
<i>T stability</i>	0.012	0.025	0.037
<i>Pressure at room temperature / Pa</i>			
<i>Uncertainty components, type B</i>			
<i>p calibration</i>	0.306	0.606	0.903
<i>Uncertainty components, type A</i>			
<i>p stability</i>	0.003	0.003	0.004
<i>Combined standard uncertainty / Pa</i>			
HPC	0.617	1.188	1.836

4 The symbol “-” means the value lies below 0.001 Pa.

5

## 1 **References**

- 2 1. B. Gao, L. Pitre, E.C. Luo, et al. Feasibility of primary thermometry using refractive  
3 index measurements at a single pressure, *Measurement* 103 (2017) 258-262.
- 4 2. P.M.C. Rourke, NRC microwave refractive index gas thermometry implementation  
5 between 24.5 K and 84 K. *Int. J. Thermophys.* 38 (2017) 1-27.
- 6 3. L. Pitre, M.R. Moldover, W.L. Tew Acoustic thermometry: new results from 273 K to  
7 77 K and progress towards 4 K, *Metrologia* 43(1) (2006) 142-162.
- 8 4. B. Gao, C.Z. Pan, L. Pitre, et al. Chinese SPRIGT realizes high temperature stability in  
9 the range of 5–25 K. *Science Bulletin* 63(12) (2018) 733-734.
- 10 5. B. Gao, C.Z. Pan, Y.Y. Chen et al. Realization of an ultra-high precision temperature  
11 control in a cryogen-free cryostat. *Rev. Sci. Instrum.* 89(10) (2018) 104901.
- 12 6. H.Y. Zhang, W.J. Liu, B. Gao, et al. A high-stability quasi-spherical resonator in  
13 SPRIGT for microwave frequency measurement at low temperatures. *Science Bulletin*  
14 64 (2019) 286-288.
- 15 7. D.X. Han, B. Gao, H. Chen, et al. Ultra-stable pressure is realized for Chinese single  
16 pressure refractive index gas thermometry in the range 30–90 kPa. *Science Bulletin* 63  
17 (2018) 1601-1603.
- 18 8. C. Meyer, M. Reilly. Realization of the ITS-90 at the NIST in the range 0,65 K to 5,0 K  
19 using the <sup>3</sup>He and <sup>4</sup>He vapour-pressure thermometry. *Metrologia* 33(4) (1996) 383-389.
- 20 9. K.D. Hill. Realizing the ITS-90 below 4.2 K at the National Research Council of  
21 Canada. *Metrologia* 39(1) (2002) 41-49.
- 22 10. A. Peruzzi, R. Bosma, M.J. de Groot, et al. <sup>4</sup>He interpolating constant-volume gas  
23 thermometry in the range 3.0 K to 24.5561 K. *Metrologia* 47(3) (2010) 325-333.
- 24 11. D.N. Astrov, L.B. Beliansky, Y.A. Dedikov, S.P. Polunin, A.A. Zakharov Precision gas  
25 thermometry between 2.5 K and 308 K. *Metrologia* 26(3) (1989) 151-166.

- 1 12. F. Sparasci, L. Pitre, D. Truong, L. Risegari. Realization of a  $^3\text{He}$ – $^4\text{He}$  Vapor-Pressure  
2 Thermometer for Temperatures between 0.65 K and 5 K at LNE-CNAM. *Int. J.*  
3 *Thermophys.* 2011, 32(1-2): 139-152.
- 4 13. F. Pavese, G.M.M. Beciet. *Modern gas-based temperature and pressure measurements.*  
5 Springer Science & Business Media, 2012.
- 6 14. P.P.M. Steur and F. Pavese “Recent progress with the IMG3  $^3\text{He}$  gas thermometer”,  
7 19th International Congress of Refrigeration, The Hague, Netherlands, August 20-25  
8 1995, poster B53 in *Physica B+C*, Proceedings vol. IIIb, 1241-1246 (1995).
- 9 15. Y.Y. Chen, H.Z. Zhang H, Y.N. Song, et al. Thermal response characteristics of a  
10 SPRIGT primary thermometry system. *Cryogenics* 97 (2019) 1-6.
- 11 16. C. Pan, T. Zhang, J. Wang, Y. Zhou. CFD study of heat transfer and pressure drop for  
12 oscillating flow in helical rectangular channel heat exchanger. *Int. J. Thermal Sciences*  
13 129 (2018) 106-114.
- 14 17. Y.P. Banjare, R.K Sahoo, S.K Sarangi. CFD simulation of a Gifford–McMahon type  
15 pulse tube refrigerator. *Int. J. Thermal Sciences* 48(12) (2009) 2280-2287.
- 16 18. L. Wang, T. Yan, J. Wang, et al. CFD investigation on thermodynamic characteristics  
17 in liquid hydrogen tank during successive varied-gravity conditions. *Cryogenics* 103  
18 (2019) 102973.
- 19 19. ANSYS Academic (Version: 19.2) [https://www.ansys.com/en-in/academic/free-](https://www.ansys.com/en-in/academic/free-student-products)  
20 [student-products](https://www.ansys.com/en-in/academic/free-student-products).
- 21 20. Eric W. Lemmon, Marcia L. Huber, Mark O. McLinden. *NIST Reference Fluid*  
22 *Thermodynamic and Transport Properties—REFPROP Version 9.1* (2013)
- 23 21. E.D. Marquardt, J.P. Le, R. Radebaugh. *Cryogenic material properties*  
24 *database//Cryocoolers 11.* Springer, Boston, MA, 2002: 681-687.



- 1 22. F. Sharipov, Data on the velocity slip and temperature jump on a gas-solid interface, J.  
2 Phys. Chem. Ref. Data 40, (2011) 023101.
- 3 23. J. Ferziger, M. Peric. Computational method for fluid dynamics, Springer: Berlin, 2002.
- 4 24. G. H. Schiroky, F. Rosenberger. Free convection of gases in a horizontal cylinder with  
5 differentially heated end walls. INT J HEAT MASS TRAN 27.4 (1984): 587-598.
- 6 25. J.W. Schmidt, R.M. Gavioso, E.F. May, M.R. Moldover Polarizability of helium and  
7 gas metrology. Phys. Rev. Lett. 98(25) (2007) 254504.
- 8 26. P.M.C. Rourke, C. Gaiser, B. Gao, et al. Refractive-index gas thermometry. Metrologia,  
9 56(3) (2019) 032001.
- 10 27. N.J. Simon, E.S. Drexler, R.P. Reed, Properties of Copper and Copper Alloys at  
11 Cryogenic Temperatures (NIST Monograph 177, National Institute of Standards and  
12 Technology, Boulder, CO 1992)
- 13 28. NIST Cryogenic Materials Properties Database, OFHC Copper (UNS C10100/C10200)  
14 entry, revised 02/03/2010.
- 15 29. C Gaiser, B Fellmuth. Polarizability of helium, neon, and argon: new perspectives for  
16 gas metrology. Phys. Rev. Lett. 120(12) (2018) 123203.
- 17 30. L.W. Bruch, F. Weinhold. Nuclear motion and Breit–Pauli corrections to the  
18 diamagnetism of atomic helium. J Chem Phys 117(7) (2002) 3243-3247 and Erratum J.  
19 Chem. Phys. 119, (2003) 638.
- 20 31. M.R. Moldover, R.M. Gavioso, J.B. Mehl et al. Acoustic gas thermometry. Metrologia  
21 51(1) (2014) R1–R19.
- 22 32. Katherine R.S. Shaul, Andrew J. Schultz, David A. Kofke. Path-integral Mayer-  
23 sampling calculations of the quantum Boltzmann contribution to virial coefficients of  
24 helium-4. J. Chem. Phys. 137(18) (2012) 184101.

- 1 33. K.H. Berry NPL-75: a low temperature gas thermometry scale from 2.6 K to 27.1 K.  
2 Metrologia 15(2) (1979) 89-115.
- 3 34. J. Fischer, M. De Podesta, K.D. Hill, et al. Present estimates of the differences between  
4 thermodynamic temperatures and the ITS-90. Int. J. Thermophys. 32(1-2) (2011) 12-  
5 25.
- 6 35. B. Fellmuth, J. Engert, T. Shimazaki and F. Sparasci. Guide to the Realization of the  
7 ITS-90, Chapter 3: Vapour Pressure Scales and Pressure Measurements (Sèvres: Bureau  
8 International des Poids et Mesures) 22p (1 1 2018)  
9 (<https://bipm.org/en/committees/cc/cct/guide-its90.html>)
- 10 36. J. Engert, B. Fellmuth <sup>3</sup>He Vapour-Pressure Measurements at PTB//AIP in Proc.  
11 Temperature: Its Measurement and Control in Science and Industry, Vol.7, Ed.  
12 D.C. Ripple et al. (AIP, Melville, New York) 684(1) (2003) 113-118.

## 1 **Supplementary Material**

2 The following is a derivation of the virial equation up fourth order in pressure.

3 The refractive index  $n$  is related to the relative dielectric permittivity  $\varepsilon_r$  and relative magnetic  
4 permeability  $\mu_r$  via

$$5 \quad n = \sqrt{\varepsilon_r \mu_r}. \quad (\text{A.1})$$

6 The virial equation for the relative dielectric permittivity is:

$$7 \quad \frac{\varepsilon_r - 1}{\varepsilon_r + 2} \left( \frac{1}{\rho} \right) = A_\varepsilon [1 + b(T)\rho + c(T)\rho^2 + o(\rho^3)]. \quad (\text{A.2})$$

8 Thus:

$$9 \quad \frac{n^2 - \mu_r}{n^2 + 2\mu_r} = A_\varepsilon [\rho + b(T)\rho^2 + c(T)\rho^3 + o(\rho^4)]. \quad (\text{A.3})$$

10 This yields the following expression for the refractive index  $n$ :

$$11 \quad n^2 = A_\varepsilon (n^2 + 2\mu_r) [\rho + b(T)\rho^2 + c(T)\rho^3 + o(\rho^4)] + \mu_r. \quad (\text{A.4})$$

12 Replacing the expression for  $n^2$  on the right-hand side of A.4 and repeating the iteration once  
13 more, one obtains:

$$14 \quad \frac{n^2 - 1}{3\rho} = \frac{A_\varepsilon}{3} (A_\varepsilon (A_\varepsilon (A_\varepsilon (n^2 + 2\mu_r) [\rho + o(\rho^2)] + 3\mu_r) [\rho + b\rho^2 + o(\rho^3)] + 3\mu_r) [\rho + b\rho^2 + c\rho^3 +  
15 \quad o(\rho^4)] + 3\mu_r) (1 + b\rho + c\rho^2 + o(\rho^3)) + \frac{\mu_r - 1}{3\rho}. \quad (\text{A.5})$$

16 For the relative magnetic permeability, assuming that  $B_\mu \equiv 0$  [30], the analogous equation to

17 A.2 is:

$$18 \quad \frac{\mu_r - 1}{\mu_r + 2} = A_\mu \rho \quad (\text{A.6})$$

19 so,

$$20 \quad \mu_r = 1 + A_\mu \rho (\mu_r + 2). \quad (\text{A.7})$$

21 Substituting A.7 into itself and repeating the iteration twice more, one obtains:

$$22 \quad \mu_r = 1 + A_\mu \rho \left( 1 + A_\mu \rho \left( \left( 1 + A_\mu \rho (\mu_r + 2) \right) + 2 \right) + 2 \right) = 1 + 3A_\mu \rho + 3A_\mu^2 \rho^2 + 3A_\mu^3 \rho^3 + o(\rho^4).  
23 \quad (\text{A.8})$$

24 By inserting the following equation and A.8 into A.5,

$$1 \quad n^2 + 2\mu_r = 3 + o(\rho) \quad (\text{A.9})$$

2 when the cross terms items such as  $A_\mu A_\varepsilon$  and those of order higher than  $A_\mu^2$  are omitted, the  
3 following equation relating refractive index and density can be obtained:

$$4 \quad \frac{n^2-1}{3\rho} = (A_\varepsilon + A_\mu) + (A_\varepsilon^2 + B_\varepsilon)\rho + (A_\varepsilon^3 + 2A_\varepsilon B_\varepsilon + C_\varepsilon)\rho^2 + (A_\varepsilon^4 + 3A_\varepsilon^2 B_\varepsilon + 2A_\varepsilon C_\varepsilon + B_\varepsilon^2)\rho^3 +$$

$$5 \quad o(\rho^4). \quad (\text{A.7})$$

6 On the other hand, from the virial equation of state:

$$7 \quad \frac{p}{RT} = \rho + B\rho^2 + C\rho^3 + D\rho^4 + o(\rho^5). \quad (\text{A.8})$$

8 one can obtain the equations below:

$$9 \quad \left\{ \begin{array}{l} \frac{p^2}{R^2 T^2} = (\rho + B\rho^2 + C\rho^3 + D\rho^4 + o(\rho^5))^2 = \rho^2 + 2B\rho^3 + B^2\rho^4 + 2C\rho^4 + o(\rho^5) \\ \frac{p^3}{R^3 T^3} = (\rho + B\rho^2 + C\rho^3 + D\rho^4 + o(\rho^5))^3 = \rho^3 + 3B\rho^4 + o(\rho^5) \\ \frac{p^4}{R^4 T^4} = (\rho + B\rho^2 + C\rho^3 + D\rho^4 + o(\rho^5))^4 = \rho^4 + o(\rho^5). \end{array} \right. \quad (\text{A.9})$$

10 Rearranging equations A.8 and A.9, one obtains:

$$11 \quad \left\{ \begin{array}{l} \rho = \frac{p}{RT} - B\rho^2 - C\rho^3 - D\rho^4 - o(\rho^5) \\ \rho^2 = \frac{p^2}{R^2 T^2} - 2B\rho^3 - B^2\rho^4 - 2C\rho^4 - o(\rho^5) \\ \rho^3 = \frac{p^3}{R^3 T^3} - 3B\rho^4 - o(\rho^5) \\ \rho^4 = \frac{p^4}{R^4 T^4} - o(\rho^5). \end{array} \right. \quad (\text{A.10})$$

12 Finally, substituting equation A.10 into A.7 and simplifying, the virial equation up to fourth  
13 order in pressure becomes:

$$14 \quad n^2 - 1 = (A_\varepsilon + A_\mu) \frac{3p}{RT} + (A_\varepsilon^2 + B_\varepsilon - A_\varepsilon B - A_\mu B) \frac{3p^2}{R^2 T^2} + (A_\varepsilon^3 + 2A_\varepsilon B_\varepsilon + C_\varepsilon - 2A_\varepsilon^2 B - 2B_\varepsilon B +$$

$$15 \quad 2A_\varepsilon B^2 + 2A_\mu B^2 - A_\varepsilon C - A_\mu C) \frac{3p^3}{R^3 T^3} + (A_\varepsilon^4 + 3A_\varepsilon^2 B_\varepsilon + B_\varepsilon^2 + 2A_\varepsilon C_\varepsilon - A_\varepsilon^2 B^2 - B_\varepsilon B^2 + A_\varepsilon B^3 +$$

$$16 \quad A_\mu B^3 - 2A_\varepsilon^2 C - 2B_\varepsilon C + 2A_\varepsilon BC + 2A_\mu BC - A_\varepsilon D - A_\mu D - 3A_\varepsilon^3 B - 6A_\varepsilon B_\varepsilon B - 3C_\varepsilon B + 6A_\varepsilon^2 B^2 +$$

$$17 \quad 6B_\varepsilon B^2 - 6A_\varepsilon B^3 - 6A_\mu B^3 + 3A_\varepsilon BC + 3A_\mu BC) \frac{3p^4}{R^4 T^4} + o(p^5). \quad (\text{A.11})$$

18  
19  
20  
21